Published in final edited form as:
NMR Biomed. 2018 September ; 31(9): e3963. doi:10.1002/nbm.3963.

Wireless Amplified NMR Detector (WAND) for Improved Visibility of Image Contrast in Heterogeneous Lesions

Xianchun Zeng[1,2,3], **Shengqiang Xu**[3], **Changyong Cao**[4], **Jian Wang**[1,*], and **Chunqi Qian**[3,*]

[1]Department of Radiology, Southwest Hospital, Army Medical University, Chongqing, China

[2]Department of Radiology, Guizhou Provincial People's Hospital, Guiyang, China

[3]Department of Radiology, Michigan State University, East Lansing, MI, USA

[4]Laboratory of Soft Machines and Electronics, School of Packaging, Departments of Mechanical, Electrical and Computer Engineering, Michigan State University, East Lansing, MI, USA

Abstract

To demonstrate the capability of a **W**ireless **A**mplifier **N**MR (Nuclear Magnetic Resonance) **D**etector (WAND) to improve the visibility of lesion heterogeneity without the use of exogenous contrast agents, a cylindrically-symmetric WAND was constructed to sensitively detect and simultaneously amplify MR signals emitted from adjacent tissues. Based on the design of 2-leg high-pass birdcage coil, this WAND could be activated by a pumping field aligned along the main field (B_0), without perturbing MR signal reception. Compared with an equivalent pair of external detectors, the WAND could achieve more than 10-fold gain for immediately adjacent regions. Even for regions with 3.4-radii distance separation from the detector's cylindrical center, the WAND was at least 1.4-fold more sensitive than an equivalent pair of surface arrays or at least 2-fold more sensitive than a single-sided external surface detector. When the WAND was inserted into a rat's rectum to observe adjacent tumors implanted beneath the mucosa, it could enhance the detection sensitivity of lesion regions, thus enlarge the observable signal difference between heterogeneous tissues and clearly identify lesion boundaries as continuous lines in the intensity gradient profile. Hyperintense regions observable by the WAND existed due to higher levels of blood supply, which was indicated by a similar pattern of signal enhancement after contrast agent administration. By better observing the endogenous signal contrast, the endoluminal WAND could characterize lesions without the use of exogenous contrast agents, thus reduce contrast-induced toxicity.

Keywords

Endo-cavity; Cylindrical; Symmetric; Wireless; Amplified; Detector; Endogenous; Contrast; Endo-cavity detector; wireless transmission; integrated amplifier; endogenous contrast; sensitivity enhancement

---

Correspondence: Jian Wang, 30 Gaotanyan Rd, Chongqing, China, 400038, Tel: +86 (23) 68754419; Fax: +86 (23) 65463026, wangjian_811@yahoo.com, Chunqi Qian, 846 Service Rd, East Lansing, MI, 48824, Tel: +1 (517) 884-3292; Fax: +1 (517) 432-2849, qianchu1@msu.edu.

Introduction

Intravenous contrast agents (1) are widely used to identify lesions rich in blood supply, by virtue of their ability to modulate MR signal intensities through relaxation enhancement (2). However, some of the well-accepted contrast agents have now been found to have the undesirable side effects of tissue retention (3,4) and toxicity (5,6). To characterize lesions without contrast agents, it is possible to utilize the endogenous signal contrast created by elevated levels of blood supply in hyper-permeable lesions or by reduced levels of blood supply in fibrous tissues. But due to the limited sensitivity of conventional Magnetic Resonance Imaging (MRI) detectors, the endogenous contrast can be too weak to observe, especially for regions that are deep-lying inside the body. Recently, it has been demonstrated that the detection sensitivity of deep-lying tissues can be greatly enhanced by a Wireless Amplified NMR Detector (WAND) (7–11). This method is based on the well-known concept that a smaller detector has better local sensitivity when placed adjacent to the region of interest (12). But instead of relying on connection wires or passive inductive coupling (13–16) that are either inconvenient or inefficient to transmit MR signals emitted from regions deep-lying inside the body, the WAND can sensitively detect and simultaneously amplify weak MR signals before efficiently broadcasting them to the external world. Aided by this sensitivity-enhanced detector, individual glomeruli could be clearly identified as hyperintense spots in T_1-weighted images (17), where the signal difference between blood-rich glomeruli and water-rich renal tubules were directly observable by *in situ* signal amplification. Although the WAND was initially developed as an implantable detector, it has been re-engineered with cylindrical shape for non-surgical use inside the digestive tract (18), in a similar fashion as gastrointestinal endoscopy. But unlike an endoscopic camera whose field of view is confined inside intestinal lumens, the endoscopic WAND can sensitively detect signals emitted from extraluminal regions and clearly observe vascular walls that are deep-lying inside the body. In this work, we are going to describe in detail the design consideration and the detection performance of a cylindrically symmetric endo-luminal detector. For extra-luminal regions that are within 3.4-radii from the WAND's cylindrical center, this detector can significantly enhance the detection sensitivity, enabling improved visibility of endogenous signal contrast inside heterogenous tumors implanted beneath rats' rectum mucosa. This tumor model is created to mimic extraluminal metastasis that was difficult to observe by ordinary optical endoscopy. Compared with external detection, the WAND can amplify the observable signal difference between heterogeneous tissues, enabling better identification of fine structure details inside heterogeneous tumors. The similar pattern of signal enhancement after contrast agent administration indicates that endogenous contrast exists due to higher levels of blood supply. Although this work is performed as a proof-of-concept demonstration for implanted tumors that are relatively easy to access, future work will include robotic delivery of the WAND inside the tortuous GI tract to sensitively observe multiple deep-lying organs, such as the pancreas, kidney, aorta and abdominal lymph nodes.

Experimental

Detector fabrication

Compared with conventional endo-cavity coils (19–21), the WAND can operate without batteries or wired connections, enabling convenient use inside confined body cavities. The operating principle of the WAND is also distinct from that of wireless chargers because the WAND can directly convert wirelessly harvested energy into amplified MR signals (7), without going through the intermediate stage of direct current that will take up extra space. With better cylindrical symmetry over its recent predecessor (22), this improved version of WAND can be activated by a longitudinal pumping field that has reduced interference with MR signal reception. As shown in Fig. 1a, the WAND is constructed by mounting 0.2-mm diameter copper wires on a 4.9-mm diameter cylinder to create a circuit pattern with two identical legs soldered with two identical end-rings. Separated by a distance of 11.4 mm, both end-rings are split by a pair of nonlinear capacitors (DB2S30800L, Panasonic). As a result, the WAND has a transverse resonance mode around 301.8 MHz ($Q = 48$) and a longitudinal resonance mode around 605 MHz ($Q = 31$). According to the schematic diagram shown in Fig. 1b, the WAND can utilize its transverse resonance mode to receive a weak MR signal at the Larmor frequency (ω_1) and its longitudinal mode to receive a strong pumping signal at $\omega_3 \sim 2\omega_1$. The two varactors on each end ring are aligned in a head-to-tail fashion, so that they are modulated in phase by the longitudinal pumping field. Enabled by the voltage-dependent capacitance of varactors, the weak MR signal at ω_1 can mix with the strong pumping signal at ω_3 to generate an amplified output at the difference frequency $\omega_2 = \omega_3 - \omega_1$. Instead of being directly detected, this “idler” signal can mix back with the pumping signal at ω_3 (red arrow) to generate a second amplified output at ω_1 (cyan arrow) that can be directly detected by standard external detectors. It is necessary to make $|\omega_3 - 2\omega_1|$ slightly larger than the imaging bandwidth, so that the amplified MR signal at ω_1 doesn’t interfere with the “idler” output at ω_2. Because the circuit loss is compensated by energy exchange enabled by multi-stage signal mixing, the WAND will have increased gain as the pumping power increases (Fig. 1c). This increased gain is manifested by the increased quality factor, i.e. $Q_{amp}/Q_0 = R_0/(R_0 - R_{Neg})$, where the circuit resistance R_0 is partially compensated by the “negative resistance” R_{Neg} introduced by the pumping signal. When the pumping field is strong enough to provide a negative resistance that can completely overcome the circuit resistance, the WAND will self-oscillate at a single frequency. To have an amplifier with 7.5-fold gain and a large enough bandwidth at 838 kHz, it is necessary to reduce the pumping power by 0.6 dBm below its oscillation threshold.

Simulation of Specific Absorption Rate (SAR)

To evaluate the possible heating effect of the pumping field, SAR inside and outside the WAND cylinder is simulated using CST Studio (Dassault Systèmes, France), To reduce computational burden, the detector circuitry was modeled as a two-leg high-pass birdcage coil soaked inside a uniform medium ($\varepsilon = 1$, $\sigma = 0.59$ S/m). Each leg of the detector was modeled to have an excitation port whose excitation power was adjusted to obtain a peak voltage of 0.044-V across each varactor on the end-ring, enabling ± 2.1% modulation of the varactor’s capacitance. According to the simple relation ($M = 1/Q$) between the modulation index M and the detector’s quality factor Q (7), an M of 2.1% would completely compensate for the energy loss of the resonator with a Q of 48 at its lower resonance mode. As shown by the axial (Fig. 1e) and longitudinal (Fig. 1f) SAR profiles, there is non-negligible SAR value only inside a narrow region around the end-ring varactor. Within this narrow region, the highest SAR is only 0.64 W/kg, which is still below the average whole-body SAR recommended by IEC 60601-2-33. According to the proportional relationship between the temperature rise ΔT and the SAR (23), i.e. $\Delta T/\Delta t = \mathrm{SAR}/C_p$, an SAR of 0.64 W/kg corresponds to a temperature rise of 0.16 mK per second, assuming the tissue specific heat C_p to be ~4 kJ kg^{-1} K^{-1}. This is equivalent to a small temperature rise of 0.5 K after continuously pumping for 52 mins (a time frame much longer than any MRI experiments). In fact, this small temperature rise could be further reduced by turning off the pumping field during the recycle delay.

MRI experiments

All images were acquired with fast spin-echo sequences, using TR/TE=1000/8.5 ms, 90° flip angle, 30 × 30 mm^2 FOV, 256 × 256 matrix, 50 kHz bandwidth, NA = 1. To improve detection sensitivity, the WAND was inserted into the detection object placed above a rectangular surface coil (28 × 28 mm). The distance separation between the WAND's cylindrical center and the external detector was ~22 mm. A single-turn loop mounted around a green plastic cylinder (Fig. 1d) was aligned along the static magnetic field B_0 to wirelessly provide the pumping field. The entire assembly was inserted into the horizontal bore of a 7T magnet (Bruker Biospin). During RF excitation, the WAND was wirelessly decoupled by the excitation field that can strongly modulate the capacitance of its constituting varactors. As a result, there would be negligible RF induced heating (24) or excitation angle over-flipping as are normally encountered in inductively coupled implantable resonators (25,26). During signal reception, less than 10-mW of power was required on the pumping loop to operate the WAND at 0.6 dBm below its oscillation threshold for efficient signal amplification. This level of pumping power would induce negligible heating in the sample, as confirmed by non-observable temperature rise measured by a rectal temperature probe (Small Animal Instruments, NY) inserted near the WAND. For sensitivity comparison, images were also obtained by the external detector in the absence of the WAND, and by an internal loop coil of the same dimension as the WAND but with a direct wire connection to the scanner.

All animal experiments were performed in accordance with guidelines approved by the Institutional Animal Care and Use Committee at Michigan State University. Each rat (Charles River) weighing around 200 g received 25 million HT29 tumor cells. These cells were grown in McCoy's 5A medium (Sigma-Aldrich) supplemented with 0.22 g/L L-glutamine and maintained in 5% CO_2 atmosphere at 37°C for 2–3 days, until reaching the confluency level of 90%. After being digested by 0.25% trypsin (Invitrogen) for 10 mins, HT29 cells were pelleted at 1500 rpm and re-suspended in phosphate-buffered saline for injection. From two days before tumor cell implantation, the rat received one intraperitoneal bolus of cyclosporine at 35 mg/kg/day for 6 days, which can suppress the rat's immune system and promote tumor growth (27). One month after tumor cell implantation, the rat was anesthetized with isoflurane and secured in the supine position for MR imaging with the WAND inserted inside its rectum. The insertion depth of the WAND was manually adjusted by an insertion rod until the tumor appeared inside the active region of the WAND in MR images. After the tumor was imaged by the WAND with elevated sensitivity, it was imaged again by the external detector after the WAND was removed. To identify the underlying mechanism of endogenous image contrast, pre-contrast images were also compared with post-contrast images obtained after intravenous administration of MultiHance (Bracco Diagnostics) at 0.125 mmol/kg of body weight. A similar pattern of hyperintensity after contrast agent administration could indicate that the endogenous image contrast observable by the WAND existed due to higher levels of blood supply.

Image processing by Matlab

To demonstrate the sensitivity advantage of the WAND in a water phantom, relative sensitivity maps were obtained by dividing images acquired using the WAND with reference images acquired using an equivalent pair of external detectors. Both images were normalized to the same noise floor. Because the scanner only has one plug-in connector for a single-channel user coil, reference images were obtained by summing up individual images acquired with the external detector placed above and beneath the phantom respectively, mimicking the effect of external receiver arrays surrounding the sample.

To identify boundaries of heterogenous tumors, the intensity gradient of each pixel was calculated to identify regions with abrupt changes in signal intensity. Lesions with well-defined boundaries are surrounded by continuous lines representing large intensity gradients. Conversely, lesions with fuzzy boundaries are surrounded by discontinuous lifnes representing smaller intensity gradients.

Results

Fig. 2a1 and 2b1 show the transverse and longitudinal images acquired across the cylindrical core of the WAND that was inserted inside a water phantom. Due to the lack of water protons in its cylindrical core, the WAND has a signal void in its center. Just like any other endo-cavity detectors, the WAND also has a distance-dependent sensitivity profile. For regions adjacent to its surface, the WAND can achieve more than 10-fold gain (Fig. 2a2) over the sensitivity of an equivalent pair of external receiver coils placed above and beneath the water phantom. For regions farther away, the WAND can still maintain its sensitivity advantage. Even when the distance separation from the WAND's cylindrical center is 3.4-times the detector's own radius, the WAND is at least 1.4-fold more sensitive than a pair of external detectors, or equivalently, at least 2-fold more sensitive than a single-sided external detector. This level of sensitivity gain is mostly maintained over a 12-mm region in the longitudinal direction (Fig. 2b2). Although slices passing through the WAND's cylindrical core have relatively steep sensitivity profiles, slices outside the WAND's cylindrical core have much smoother profiles. For example, for a longitudinal slice that is 6-mm (about 2.4-radii) away from the WAND's cylindrical center (Fig. 2c1), the WAND has a sensitivity gain of 2.7 ± 0.5 over a $10.5 \times 8.0\text{-mm}^2$ region (Fig. 2c2). According to the flip angle maps in Figs. 2a3, 2b3 and 2c3, the WAND introduces little perturbation to the uniformity of RF excitation in its active detection region outside its cylindrical core, owing to the efficient modulation of its constituting varactors by RF excitation fields. Compared with images obtained by a directly connected coil of the same dimension (Figs. 2a4, 2b4 and 2c4), images obtained by the WAND have similar enhancement patterns with only slightly smaller effective ranges than the directly connected coil (Figs. 2a5, 2b5, 2c5).

Because of their smoothness, longitudinal slices were first acquired outside the WAND's cylindrical core to demonstrate the improved visibility of lesion heterogeneity. As shown in Fig. 3a1, the lesion node in the pre-contrast image is barely visible by the external detector. This is corroborated by the fuzzy boundary line defined in the intensity gradient profile (Fig. 3a2) and by the modest difference between hyper-intense peaks inside the lesion region and the enclosed valleys highlighted by red dashed lines (Fig. 3a3). With the WAND inserted nearby for *in situ* amplification, multiple hypo-intense spots are clearly visible inside the lesion node (Fig. 3b1) with well-defined boundary (Fig. 3b2), owing to the 5-fold (± 0.8) gain of normalized intensity (Fig. 3b3). Because the WAND has a fixed position inside the rectum to receive constant pumping power, amplified images have negligible motion artifact. MultiHance administration can also improve the visibility of lesion node with respect to its surroundings (Fig. 3c1). Compared with the pre-contrast image, the lesion boundary is better visualized in the gradient plot (Fig. 3c2) owing to the about 2-fold gain of normalized intensity (Fig. 3c3). The similar pattern of hyperintensity brought by contrast agent administration suggests that endogenous contrast observable by the WAND exists due to higher levels of blood supply in vascular-rich regions that are more amenable to contrast agent accumulation.

In addition to longitudinal slices outside the detector's cylindrical core, transverse slices passing through the detector's center are also useful to characterize subtle lesion nodes, such as the one with a diameter of ~1.7 mm (Fig. 4a1). When observed by the external detector placed on the rat's dorsal side, the lesion region appears as a slightly more intense node due to elevated levels of blood supply. But because of the relatively low sensitivity of the external detector, the lesion node has blurred boundaries (Fig. 4a2) and barely visible internal structures with non-obvious signal contrast in the normalized intensity plot (Fig. 4a3). When the WAND is inserted inside the rectum for sensitivity enhancement, the lesion node has much sharper boundary and a clearly visible hypo-intense spot in its center (Fig. 4b1), which probably corresponds to fibrous tissues. Compared with Fig. 4a2, the WAND can better identify lesion boundaries and hypo-intense spots enclosed inside the lesion node (Fig. 4b2), by increasing the normalized intensity by a factor of 3.0 ± 0.6 (Fig. 4b3). To attribute endogenous contrast to blood flow, the lesion node is again observed by the external detector after MultiHance administration (Fig. 4c1). Due to contrast agent accumulation, the lesion node has visible boundaries (Fig. 4c2). Its normalized intensity is enhanced by a factor of 2.0 ± 0.4 (Fig. 4c3) when compared with the pre-contrast intensity profile (Fig. 4a3). The similar pattern of hyperintensity brought by MultiHance administration again suggests that the endogenous contrast observable by the WAND results from higher levels of blood supply.

Finally, the WAND is utilized to characterize multiple lesion nodes of different sizes and shapes near the rectum, without the use of contrast agents. For example, the oval-shaped lesion (Fig. 5a1) defined by its clear boundary (Fig. 5a2) has a flake-shaped hypo-intense region in its center. Beneath the lesion is the exudation region that extends towards the muscular gap aligning approximately parallel to the long axis of the oval lesion. Meanwhile, the lesion node in Fig. 5b1 has partially defined boundaries (Fig. 5b2) at its bottom due to muscular invasion. The hypo-intense spots inside the lesion have sharp contrast with respect to their surroundings, demonstrating the effectiveness of the WAND to identify tissue heterogeneities. As another example, the gourd-shaped lesion in Fig. 5c1 has clear boundaries (Fig. 5c2), inside which is a hypo-intense line that is parallel to the lesion's long axis (Fig. 5c1). Beneath the bottom tip of the hypo-intense line is a circular node surrounded by a slightly hypo-intense ring that can be clearly identified by the WAND. Details about the lesions in the five different rats mentioned in Figs 3, 4 and 5 are summarized in Table 1.

Discussion

In this work, a Wireless Amplified NMR Detector (WAND) with improved cylindrical symmetry has been fabricated, whose effective detection range is fully characterized. Based on the design of 2-leg high-pass birdcage coil, this detector has improved cylindrical symmetry over its predecessors. Unlike previous versions of WANDs (7,22,28) that required a pumping field perpendicular to the main field B_0, the current version of WAND relies on the normally under-utilized ring resonance mode to harvest wirelessly-provided pumping energy for *in situ* signal amplification. As a result, this cylindrically-symmetric WAND can be activated by a pumping field aligned along the B_0 direction, which doesn't interfere with MR signal reception. This detection configuration is compatible with most endovascular or endo-cavity applications, where the WAND is often aligned (at least partially) along the B_0 direction by the body's natural cavity. Like any other endo-cavity detectors, the WAND has a distant-dependent sensitivity profile. Therefore, its effective range has been calibrated in this work to evaluate its detection capability for extraluminal regions. Even when the region of interest is separated from the detector's cylindrical center by 3.4-radii, the WAND is at least 1.4-fold more sensitive than a pair of external detector arrays, whose equivalent sensitivity was evaluated by adding two images that were sequentially acquired with a single-sided external detector placed beneath and above the detection object. (This image summation process is adapted to mimic the detection sensitivity of whole body array, without being limited by scanner's single-channel connector for user-developed coils.) Compared with conventional endo-cavity coils with direct wire connection, the WAND's constituting varactors have led to several favorable features, including wireless powered amplification and excitation field decoupling, both of which make the WAND convenient to operate inside the body with reduced risk of sample heating. This is corroborated by the WAND's negligible perturbation to the excitation field homogeneity and unmeasurable heating over its surrounding regions. The wireless signal interface also enables convenient switching between high-resolution imaging by internal detector and low-resolution imaging by external detector, without the need for cable rewiring.

To demonstrate the application of this wireless endo-cavity detector for tumor characterization, the WAND is non-surgically inserted inside a rat's rectum to sensitively identify the endogenous signal contrast in tumors implanted beneath the mucosa, without the use of exogenous agents. Once the WAND is delivered by an insertion rod to an endoluminal position that was close enough to the tumor, it is secured at this fixed location to receive constant pumping power and to amplify MR signals with negligible motion artifact. Compared with an external surface coil placed on the animal's dorsal side, the WAND can highlight the observable signal difference between heterogenous tissues, thus improve the visibility of lesion heterogeneity. This is evidenced by the increased intensity differences between hypointense spots and their surrounding regions in the lesion node, whose boundary can be clearly identified as continuous lines in intensity gradient profiles. (For *in vivo* images, the reference standard is a single-sided surface coil placed on the dorsal side rather than an equivalent pair of external detector because the lesion node is much closer to the dorsal side than to the abdominal side.) When the lesion region is within 3.4-raddi separation from the WAND's cylindrical center, the WAND can clearly identify lesion heterogeneity without the need for contrast agents, highlighting the endogenous image contrast between hyper-perfuse and hypo-perfuse regions, thus provide an alternative but effective way to diagnose early stage metastasis of colorectal tumors beyond the submucosal layer. By reducing the need for contrast agents, this sensitivity-enhanced detector can be even more suitable for deep-lying lesions with no or little blood supply, such as lipid-rich plaques with thin but intact fibrotic caps, where contrast agents are difficult to enter. Although the current study focuses on rodent models with tumors implanted beneath their rectum mucosa for easy access through manual insertion, future work will include automatic delivery of the WAND with a flexible catheter inside the tortuous GI tract to sensitively characterize subtle abnormalities in deep-lying organs adjacent to the GI tract, such as the pancreas (29–31), prostate (32,33), kidney (34), aorta (35) and abdominal lymph nodes (36).

In conclusion, a cylindrically symmetric endo-cavity WAND has been designed and characterized to improve the visibility of lesion heterogeneity without contrast agents, thus avoid their side effects of tissue retention and toxicity. In addition to implantable and interventional applications, this compact design of an integrated signal amplifier may also help to improve wireless detectors placed outside the body (37–40), by further reducing their weight and power consumption for improved operation flexibility.

Acknowledgments

This research is currently supported by the NIBIB under award number R00EB016753 MSU Foundation Strategic Partnership Grant Program (16-SPG-Full-3236) and the Department of Radiology at Michigan State University. Dr. Zeng greatly acknowledges the generous support by the CSC fellowship. The content of this paper does not necessarily represent official views of the NIH.

Abbreviations used

WAND	Wireless Amplified NMR Detector
MRI	Magnetic Resonance Imaging
NMR	Nuclear Magnetic Resonance
RF	Radiofrequency
SAR	Specific Absorption Rate

References

1. Caravan P, Ellison JJ, McMurry TJ, Lauffer RB. Gadolinium(III) chelates as MRI contrast agents: Structure, dynamics, and applications. Chem Rev. 1999; 99(9):2293–2352. [PubMed: 11749483]

2. Pirovano G, Vanzulli A, Marti-Bonmati L, Grazioli L, Manfredi R, Greco A, Holzknecht N, Daldrup-Link HE, Rummeny E, Hamm B, Arneson V, Imperatori L, Kirchin MA, Spinazzi A. Evaluation of the accuracy of gadobenate dimeglumine-enhanced MR imaging in the detection and characterization of focal liver lesions. Am J Roentgenol. 2000; 175(4):1111–1120. [PubMed: 11000175]
3. Semelka RC, Ramalho J, Vakharia A, AlObaidy M, Burke LM, Jay M, Ramalho M. Gadolinium deposition disease: Initial description of a disease that has been around for a while. Magn Reson Imaging. 2016; 34(10):1383–1390. [PubMed: 27530966]
4. Zhang Y, Cao Y, Shih GL, Hecht EM, Prince MR. Extent of Signal Hyperintensity on Unenhanced T1-weighted Brain MR Images after More than 35 Administrations of Linear Gadolinium-based Contrast Agents. Radiology. 2017; 282(2):516–525. [PubMed: 27513848]
5. Thomsen HS, Morcos SK, Dawson P. Is there a causal relation between the administration of gadolinium based contrast media and the development of nephrogenic systemic fibrosis (NSF)? Clin Radiol. 2006; 61(11):905–906. [PubMed: 17018301]
6. Rogosnitzky M, Branch S. Gadolinium-based contrast agent toxicity: a review of known and proposed mechanisms. Biometals : an international journal on the role of metal ions in biology, biochemistry, and medicine. 2016; 29(3):365–376.
7. Qian C, Murphy-Boesch J, Dodd S, Koretsky A. Sensitivity enhancement of remotely coupled NMR detectors using wirelessly powered parametric amplification. Magn Reson Med. 2012; 68(3):989–996. [PubMed: 22246567]
8. Qian CQ, Yu X, Chen DY, Dodd S, Bouraoud N, Pothayee N, Chen Y, Beeman S, Bennett K, Murphy-Boesch J, Koretsky A. Wireless Amplified Nuclear MR Detector (WAND) for High-Spatial-Resolution MR Imaging of Internal Organs: Preclinical Demonstration in a Rodent Model. Radiology. 2013; 268(1):228–236. [PubMed: 23392428]
9. Syms RRA, Solymar L, Young IR. Three-frequency parametric amplification in magneto-inductive ring resonators. Metamaterials. 2008; 2:122–134.
10. Syms RRA, Floume T, Young IR, Solymar L, Rea M. Parametric Amplification of Magnetic Resonance Images. Ieee Sensors Journal. 2012; 12(6):1836–1845.
11. Martius S, Heid O, Vester M, Biber S, Nistler J. Wireless local coil signal transmission using a parametric upconverter. Proc Intl Soc Mag Reson Med. 2009:2934.
12. Olson DL, Peck TL, Webb AG, Magin RL, Sweedler JV. High-Resolution Microcoil 1H-Nmr for Mass-Limited, Nanoliter-Volume Samples. Science. 1995; 270(5244):1967–1970.
13. Hoult DI, Tomanek B. Use of mutually inductive coupling in probe design. Concepts in Magnetic Resonance (magnetic resonance engineering). 2002; 15(4):262–285.
14. Wirth ED 3rd, Mareci TH, Beck BL, Fitzsimmons JR, Reier PJ. A comparison of an inductively coupled implanted coil with optimized surface coils for in vivo NMR imaging of the spinal cord. Magn Reson Med. 1993; 30(5):626–633. [PubMed: 8259063]
15. Schnall MD, Barlow C, Subramanian VH, Leigh JS. Wireless Implanted Magnetic-Resonance Probes for in vivo NMR. J Magn Reson. 1986; 68(1):161–167.
16. Quick HH, Zenge MO, Kuehl H, Kaiser G, Aker S, Massing S, Bosk S, Ladd ME. Interventional magnetic resonance angiography with no strings attached: Wireless active catheter visualization. Magnetic Resonance in Medicine. 2005; 53(2):446–455. [PubMed: 15678524]
17. Qian C, Yu X, Pothayee N, Dodd S, Bouraoud N, Star R, Bennett K, Koretsky A. Live nephron imaging by MRI. Am J Physiol Renal Physiol. 2014; 307(10):F1162–1168. [PubMed: 25186296]
18. Zeng X, Chen L, Wang C, Wang J, Qian C. Wireless MRI Colonoscopy for Sensitive Imaging of Vascular Walls. Sci Rep. 2017; 7(1):4228. [PubMed: 28652614]
19. Ackerman JL, Nevo E, Zucker EJ, Poitzsch AJ, Vandenberg K, Zhigalin A, Fetics B. MR Endoscope with Software-Controlled Tuning, Device Tracking and Video. Proc Intl Soc Mag Reson Med. 2011; 19:1759.
20. Zhang X, Martin A, Jordan C, Lillaney P, Losey A, Pang Y, Hu J, Wilson M, Cooke D, Hetts S. Design of catheter radio frequency coils using coaxial transmission line resonators for interventional neurovascular MR imaging. Quant Imaging Med surg. 2017; 7(2):187–194. [PubMed: 28516044]

21. Atalar E, Bottomley PA, Ocali O, Correia LCL, Kelemen MD, Lima JAC, Zerhouni EA. High resolution intravascular MRI and MRS by using a catheter receiver coil. Magn Reson Med. 1996; 36(4):596–605. [PubMed: 8892213]
22. Zeng XC, Barbic M, Chen L, Qian CQ. Sensitive Enhancement of Vessel Wall Imaging with an Endo-esophageal Wireless Amplified NMR Detector (WAND). Mag Res Med. 2017; 78(5):2048–2054.
23. Hoffmann J, Henning A, Giapitzakis IA, Scheffler K, Shajan G, Pohmann R, Avdievich NI. Safety testing and operational procedures for self-developed radiofrequency coils. NMR Biomed. 2016; 29(9):1131–1144. [PubMed: 25851551]
24. Busch M, Vollmann W, Bertsch T, Wetzler R, Bornstedt A, Schnackenburg B, Schnorr J, Kivelitz D, Taupitz M, Gronemeyer D. On the heating of inductively coupled resonators (stents) during MRI examinations. Magnetic Resonance in Medicine. 2005; 54(4):775–782. [PubMed: 16149073]
25. Kivelitz D, Wagner S, Schnorr J, Wetzler R, Busch M, Melzer A, Taupitz M, Hamm B. A vascular stent as an active component for locally enhanced magnetic resonance imaging - Initial in vivo imaging results after catheter-guided placement in rabbits. Investigative radiology. 2003; 38(3): 147–152. [PubMed: 12595794]
26. Kivelitz D, Wagner S, Hansel J, Schnorr J, Wetzler R, Busch M, Melzer A, Taupitz M, Hamm B. The active magnetic resonance imaging stent (AMRIS) - Initial experimental in vivo results with locally amplified MR angiography and flow measurements. Investigative radiology. 2001; 36(11): 625–631. [PubMed: 11606839]
27. Akhter J, Yao P, Johnson LA, Riordan SM, Morris DL. A new peritoneal carcinomatosis model in cyclosporine immunosuppressed rats. Anticancer research. 2008; 28(1A):105–108. [PubMed: 18383831]
28. Qian C, Yu X, Chen DY, Dodd S, Bouraoud N, Pothayee N, Chen Y, Beeman S, Bennett K, Murphy-Boesch J, Koretsky A. Wireless amplified nuclear MR detector (WAND) for high-spatial-resolution MR imaging of internal organs: preclinical demonstration in a rodent model. Radiology. 2013; 268(1):228–236. [PubMed: 23392428]
29. Pozzi-Mucelli RM, Rinta-Kiikka I, Wunsche K, Laukkarinen J, Labori KJ, Anonsen K, Verbeke C, Del Chiaro M, Kartalis N. Pancreatic MRI for the surveillance of cystic neoplasms: comparison of a short with a comprehensive imaging protocol. Eur Radiol. 2017; 27(1):41–50. [PubMed: 27246720]
30. Brenner R, Metens T, Bali M, Demetter P, Matos C. Pancreatic neuroendocrine tumor: Added value of fusion of T2-weighted imaging and high b-value diffusion-weighted imaging for tumor detection. Eur J Radiol. 2012; 81(5):E746–E749. [PubMed: 22386133]
31. Lotfalizadeh E, Ronot M, Wagner M, Cros J, Couvelard A, Vullierme MP, Allaham W, Hentic O, Ruzniewski P, Vilgrain V. Prediction of pancreatic neuroendocrine tumour grade with MR imaging features: added value of diffusion-weighted imaging. Eur Radiol. 2017; 27(4):1748–1759. [PubMed: 27543074]
32. Panebianco V, Sciarra A, Marcantonio A, Forte V, Biondi T, Laghi A, Catalano C. Conventional imaging and Multiparametric Magnetic Resonance (MRI, MRS, DWI, MRP) in the diagnosis of prostate cancer. Q J Nucl Med Mol Im. 2012; 56(4):331–342.
33. Lim C, Malone SC, Avruch L, Breau RH, Flood TA, Lim M, Morash C, Quon JS, Walsh C, Schieda N. Magnetic resonance for radiotherapy management and treatment planning in prostatic carcinoma. Brit J Radiol. 2015; 88(1054)
34. Michaely HJ, Sourbron S, Dietrich O, Attenberger U, Reiser MF, Schoenberg SO. Functional renal MR imaging: an overview. Abdom Imaging. 2007; 32(6):758–771. [PubMed: 17151905]
35. Lin JM, Patterson AJ, Chao TC, Zhu C, Chang HC, Mendes J, Chung HW, Gillard JH, Graves MJ. Free-breathing black-blood CINE fast-spin echo imaging for measuring abdominal aortic wall distensibility: a feasibility study. Phys Med Biol. 2017; 62(10):N204–N218. [PubMed: 28327475]
36. Arrive L, Derhy S, El Mouhadi S, Monnier-Cholley L, Menu Y, Becker C. Noncontrast Magnetic Resonance Lymphography. Journal of reconstructive microsurgery. 2016; 32(1):80–86. [PubMed: 25826439]
37. Bulumulla SB, Fiveland E, Park KJ, Foo TK, Hardy CJ. Inductively coupled wireless RF coil arrays. Magn Reson Imaging. 2015; 33(3):351–357. [PubMed: 25523607]

38. Aggarwal K, Joshi KR, Rajavi Y, Taghivand M, Pauly JM, Poon AS, Scott G. A Millimeter-Wave Digital Link for Wireless MRI. IEEE transactions on medical imaging. 2017; 36(2):574–583. [PubMed: 27810803]

39. Wei J, Liu Z, Chai Z, Yuan J, Lian J, Shen GX. A realization of digital wireless transmission for MRI signals based on 802. 11b. J Magn Reson. 2007; 186(2):358–363. [PubMed: 17433744]

40. Murakami R, Takahashi T, Yamamoto E. Nuclear magnetic resonance inspection apparatus and its method. US Patent. 5384536. 1995.

41. Cunningham CH, Pauly JM, Nayak KS. Saturated double-angle method for rapid B-1 plus mapping. Magn Reson Med. 2006; 55(6):1326–1333. [PubMed: 16683260]

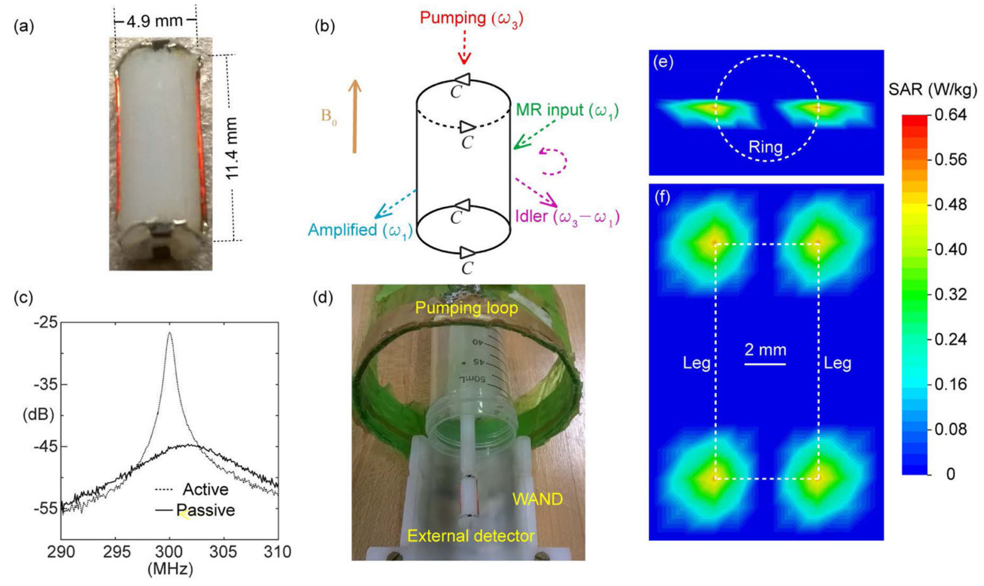

Fig. 1.

(a) The picture of an 11.4-mm long WAND made of two identical legs interlaced with two identical end-rings mounted on a 4.9-mm diameter cylinder. (b) The schematic diagram of this cylindrically symmetric detector with a horizontal (lower frequency) resonance mode and a longitudinal (higher frequency) resonance mode. (c) The S_{21} curve measured with a double pick-up loop placed adjacent to the resonator and connected to a network analyzer. Compared with the solid curve measured in the absence of pumping power, the dotted curve measured in the presence of pumping power has obvious increase in peak height and shift in peak frequency, demonstrating the effectiveness of wireless powered amplification and frequency tuning. (d) The arrangement for phantom imaging with the WAND inserted inside a water tube placed along the normal axis of a single-turn pumping loop. The distance separation between the WAND's cylindrical center and the external detector placed beneath the sample tube is about 22 mm. Based on a pumping power that was set to approximately 0.6 dB below the resonator's oscillation threshold, Specific Absorption Rate (SAR) was simulated in both the transverse (e) and longitudinal (f) cross sections. The highest SAR value adjacent to the end-ring varactors is only 0.64 W/kg, which is far below the safety value recommended by IEC 60601-2-33.

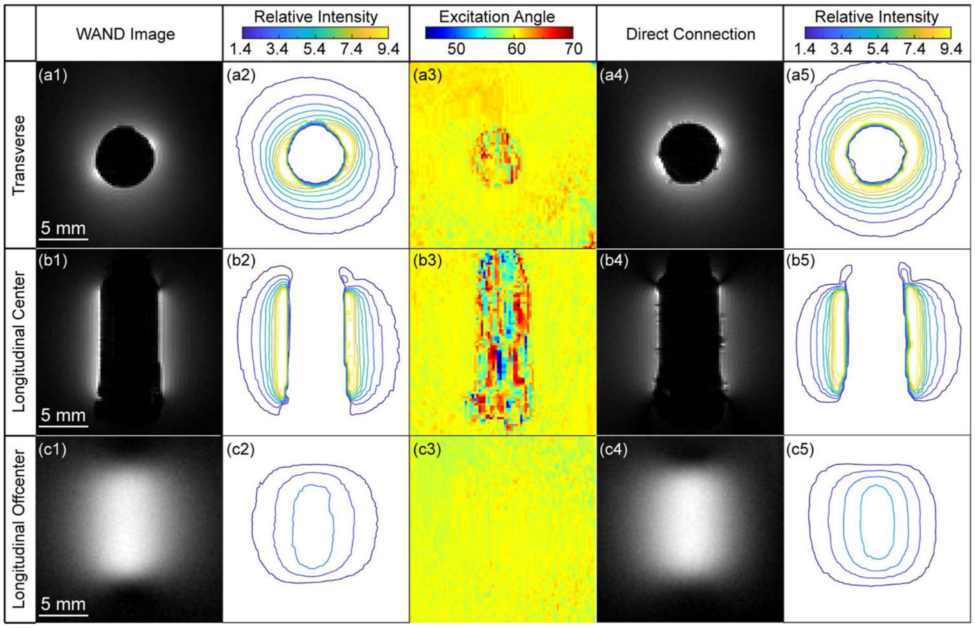

Fig. 2.

The transverse (row 1) and longitudinal (row 2) images acquired across the cylindrical core of the WAND inserted inside a water phantom, using TR/TE=1000/8.5 ms, 90° flip angle, 30 × 30 mm^2 FOV, 256 × 256 matrix, 50 kHz bandwidth, NA = 1. Row 3 shows longitudinal images acquired outside the WAND's cylindrical core, using the same acquisition parameters. Column 1 shows zoomed-in views of images acquired with active amplification. Column 2 shows the relative intensity ratio between images acquired using the amplified detector and those images acquired using an equivalent pair of external detectors placed beneath and above the phantom. Column 3 shows flip angle maps of the WAND obtained by the double angle method using 60° and 120° excitations (41), with TR = 5 s and all other parameters remaining the same as above. For sensitivity comparison, the same images acquired with a loop coil of the same dimension as the WAND but with direct wire connection are shown in column 4, whose relative intensity profiles with respect to the equivalent pair of external detectors are shown in column 5.

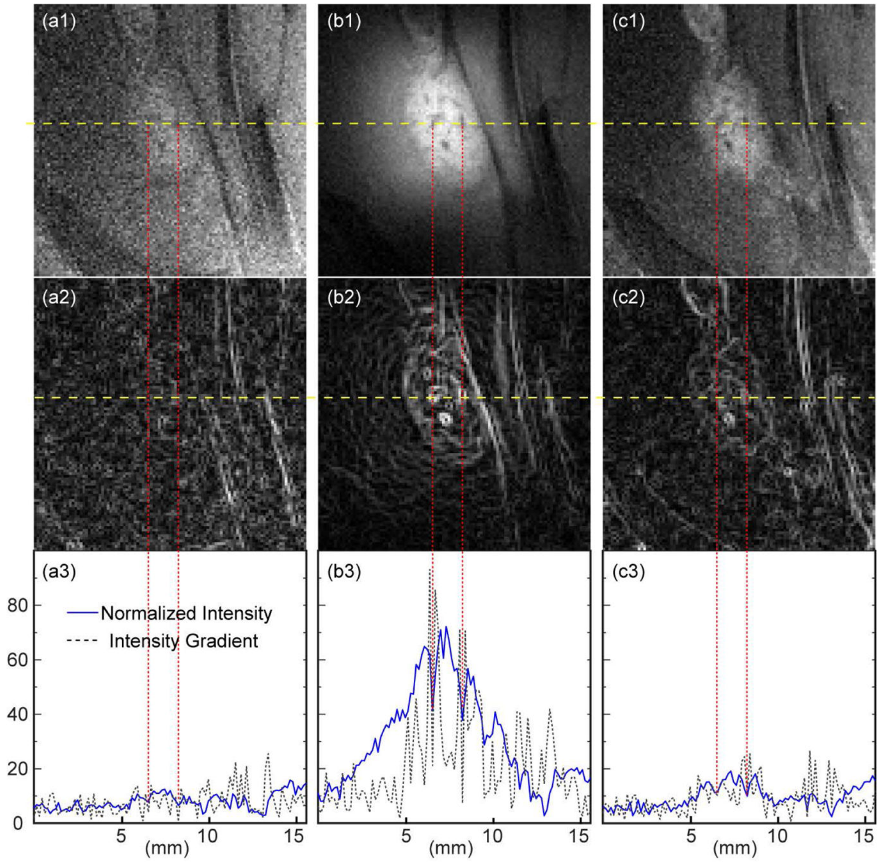

Fig. 3.

(a1) and (c1) are zoomed-in views of T_1-weighted longitudinal images acquired before and after MultiHance administration, using the external detector placed on the rat's dorsal side. (b1) is the same image acquired with the WAND inserted in the rectum to enhance the endogenous signal contrast without administration of exogenous agents. (a2), (b2) and (c2) show the intensity gradient profile evaluated for each zoomed-in view, where smooth continuous lines correspond to well-defined boundaries. (a3), (b3) and (c3) show the normalized intensity (solid blue) and intensity gradient (dotted black) plotted along the yellow dashed line passing through multiple hypointense spots inside the lesion nodes.

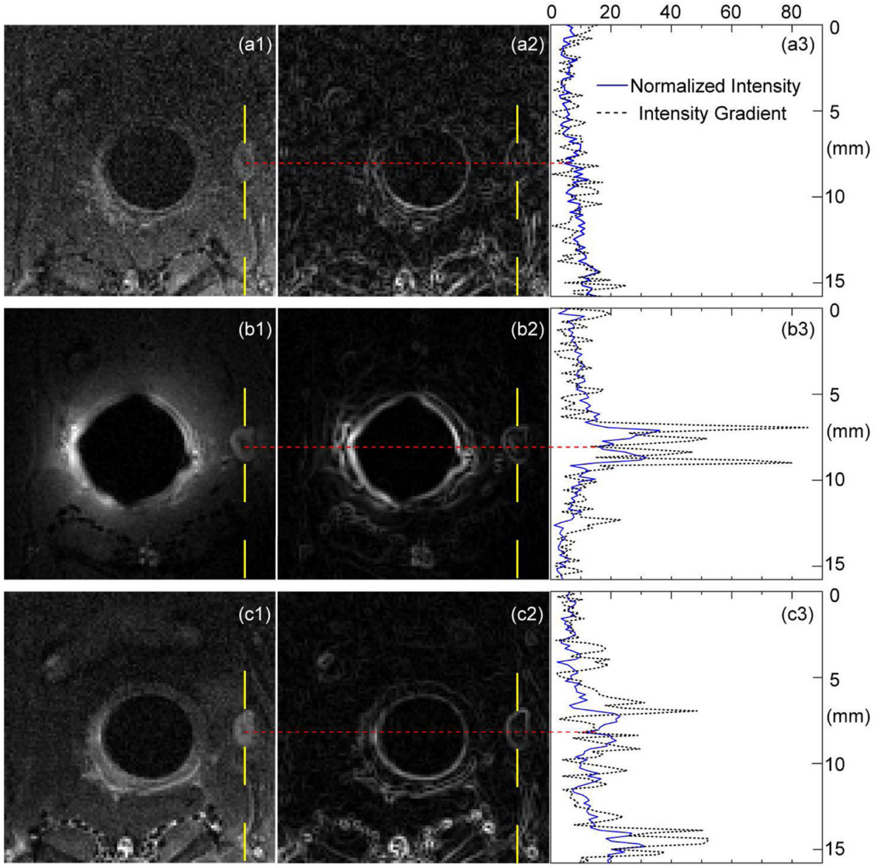

Fig. 4.

(a1) and (c1) are zoomed-in views of T_1-weighted transverse images acquired before and after MultiHance administration, using the external detector placed on the rat's dorsal side. (b1) is the same image acquired with the WAND inserted in the rectum to enhance the endogenous signal contrast without administration of exogenous agents. (a2), (b2) and (c2) show the intensity gradient profile evaluated for each zoomed-in view, where smooth continuous lines correspond to well-defined boundaries. (a3), (b3) and (c3) show the normalized intensity (solid blue) and intensity gradient (dotted black) plotted along the yellow dashed line passing through the hypointense spot inside the lesion node.

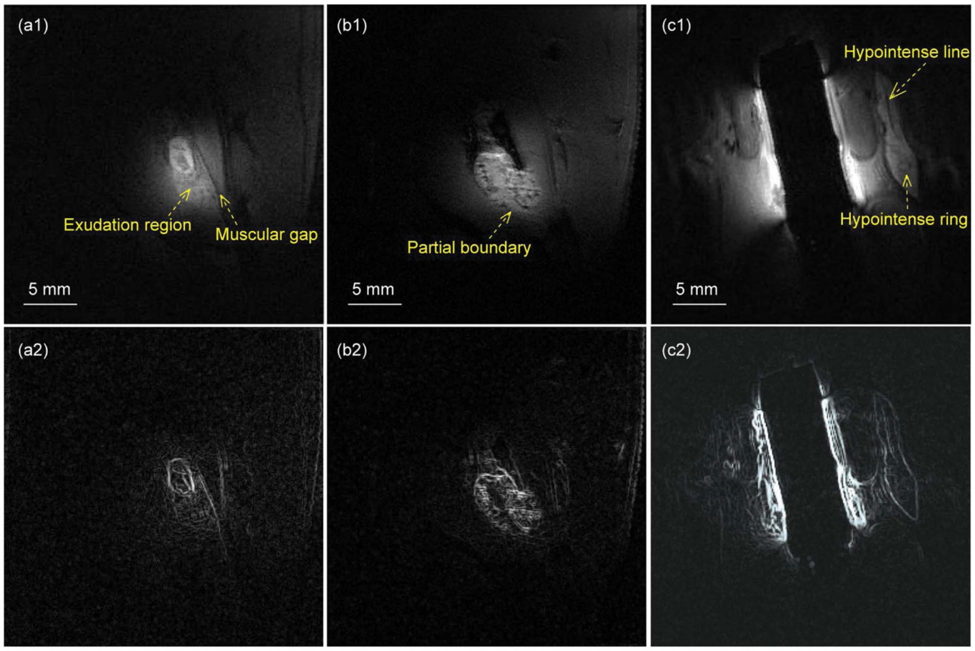

Fig. 5.

Row 1 shows a series of sensitivity-enhanced images acquired by the WAND for improved visibility of endogenous signal contrast in lesion nodes of different sizes and shapes, leading to clearly visible boundary lines in the intensity gradient profiles (row 2).

Table 1

The geometry and enhancement factor of lesions in different rats

Rat #	Fig. Label	Center-to-center*	Size & Shape	Sensitivity gain
1	Fig. 3	5 mm	7.0 × 3.8 (oval)	5.0 ± 0.8
2	Fig. 4	6.7 mm	D=1.7 (circle)	3.0 ± 0.6
3	Fig. 5a	8 mm	3.8 × 2.2 (oval)	2.2 ± 0.4
4	Fig. 5b	8 mm	6.7 × 5.3 (oval)	2.1 ± 0.3
5	Fig. 5c	9 mm	12 × 2.6 (gourd)	1.6 ± 0.3

*Center-to-center means the distance separation between the lesion node's center and the WAND's cylindrical center.